



HAL
open science

XBi₄S₇ (X = Mn, Fe): New Cost-Efficient Layered n-Type Thermoelectric Sulfides with Ultralow Thermal Conductivity

Jean-baptiste Labégorre, Agathe Virfeu, Abdelhamid Bourhim, Héloïse Willeman, Tristan Barbier, Florian Appert, Jean Juraszek, Bernard Malaman, Arthur Huguenot, Régis Gautier, et al.

► To cite this version:

Jean-baptiste Labégorre, Agathe Virfeu, Abdelhamid Bourhim, Héloïse Willeman, Tristan Barbier, et al.. XBi₄S₇ (X = Mn, Fe): New Cost-Efficient Layered n-Type Thermoelectric Sulfides with Ultralow Thermal Conductivity. *Advanced Functional Materials*, 2019, 29 (48), pp.1904112. 10.1002/adfm.201904112 . hal-02301334

HAL Id: hal-02301334

<https://normandie-univ.hal.science/hal-02301334>

Submitted on 25 Nov 2020

HAL is a multi-disciplinary open access archive for the deposit and dissemination of scientific research documents, whether they are published or not. The documents may come from teaching and research institutions in France or abroad, or from public or private research centers.

L'archive ouverte pluridisciplinaire **HAL**, est destinée au dépôt et à la diffusion de documents scientifiques de niveau recherche, publiés ou non, émanant des établissements d'enseignement et de recherche français ou étrangers, des laboratoires publics ou privés.

XBi₄S₇ (X = Mn, Fe): new cost-efficient layered *n*-type thermoelectric sulfides with ultralow thermal conductivity

Jean-Baptiste Labégorre,^{a,†} Agathe Virfeu,^{b,†} Abdelhamid Bourhim,^a Héloïse Willeman,^b Tristan Barbier,^a Florian Appert,^c Jean Juraszek,^c Bernard Malaman,^d Arthur Huguenot,^c Régis Gautier,^c Vivian Nassif,^f Pierric Lemoine,^e Carmelo Prestipino,^e Erik Elkaim,^g Lauriane Pautrot-d'Alençon,^h Thierry Le Mercier,^h Antoine Maignan,^a Rabih Al Rahal Al Orabi,^{b,i,*} Emmanuel Guilmeau^{a,*}

^a CRISMAT, CNRS, Normandie Univ, ENSICAEN, UNICAEN, 14000 Caen, France

^b Solvay, Design and Development of Functional Materials Department, Axel'One, 87 avenue des Frères Perret, 69192 Saint Fons, Cedex, France

^c Normandie Univ, UNIROUEN, INSA Rouen, CNRS, GPM, 76000 Rouen, France

^d Institut Jean Lamour, UMR 7198, CNRS, Université de Lorraine, Faculté des Sciences et Technologie, B.P. 70239, 54506 Vandœuvre-lès-Nancy Cedex, France

^e Univ Rennes, Ecole Nationale Supérieure de Chimie de Rennes, CNRS, ISCR, 35000 Rennes, France

^f Univ. Grenoble Alpes, F-38000 Grenoble, France & CNRS, Inst. NEEL, F-38042 Grenoble, France

^g Synchrotron Soleil, L'orme des Merisiers, Saint-Aubin - BP 48, F-91192 Gif-sur-Yvette cedex, France

^h Solvay, Centre de Recherches d'Aubervilliers, 52 rue de la Haie-Coq, 93308 Aubervilliers Cedex, France

ⁱ Department of Physics, Central Michigan University, Mt. Pleasant, Michigan 48879, United States

*Email : emmanuel.guilmeau@ensicaen.fr, Tel : +33 231 45 13 67

*Email : rabih.orabi@solvay.com, Tel : +33 428 27 10 80

Abstract

We report a new class of cost-efficient *n*-type thermoelectric sulfides with a layered structure, namely MnBi_4S_7 and FeBi_4S_7 . Theoretical calculations combined with synchrotron X-ray/neutron diffraction analyses reveal the origin of their electronic and thermal properties. The complex low-symmetry monoclinic crystal structure generates an electronic band structure with a mixture of heavy and light bands near the conduction band edge, as well as vibrational properties favorable for high thermoelectric performance. The low thermal conductivity can be attributed to the complex layered crystal structure and to the existence of the lone pair of electrons in Bi^{3+} . This feature combined with the relatively high power factor lead to a figure of merit as high as 0.21 (700 K) in undoped MnBi_4S_7 , making this material a promising *n*-type candidate for the low- and intermediate-temperature thermoelectric applications.

1. Introduction

Since the dawn of the 21st century, the development of renewable energies turns out to be a priority to emancipate from the polluting fossil fuels and overcome the future energy needs. Among the different technologies developed to address this societal problematic, the thermoelectricity appears as a promising energy recovery technique thanks to its versatility and ability to achieve a direct energy conversion between heat and electricity. The energy conversion efficiency of a thermoelectric material is usually quantified by the dimensionless figure of merit $ZT = S^2T/\rho\kappa$, where S is the Seebeck coefficient ($\mu\text{V K}^{-1}$), T is the absolute temperature (K), ρ is the electrical resistivity ($\Omega \text{ m}$) and κ is the thermal conductivity ($\text{W m}^{-1} \text{ K}^{-1}$).^[1] From the 1950s, efficient thermoelectric materials as Bi_2Te_3 or PbTe have been discovered and continuously improved until now, leading to high figure of merit values. However, most of these materials suffer from high costs, toxicity and elements scarcity which preclude their use for mass

consumption markets and thus limit their positive environmental impact. The emergence of new potential markets for thermoelectrics, as automotive or the Internet of Things (IoT), require higher volumes and lower prices. These new needs gradually steered the thermoelectricity toward new materials with undeniable advantages in terms of performance/cost ratio. Over the past 10 years, sulfides won fame with the discovery of multiple new affordable and eco-friendly thermoelectric materials. Among this family, numerous efficient *p*-type materials have been unveiled and optimized as tetrahedrite $\text{Cu}_{12}\text{Sb}_4\text{S}_{13}$ ($ZT \sim 0.8$ at 700 K),^[2–6] colusite $\text{Cu}_{26}\text{V}_2\text{Sn}_6\text{S}_{32}$ ($ZT \sim 0.93$ at 675 K),^[7–10] Cu_2SnS_3 ($ZT \sim 0.85$ at 723 K),^[11,12] bornite Cu_5FeS_4 ($ZT \sim 0.79$ at 550 K),^[13–16] $\text{Cu}_2\text{ZnSnS}_4$ ($ZT \sim 0.36$ at 700 K),^[17] stannoidite $\text{Cu}_8\text{Fe}_3\text{Sn}_2\text{S}_{12}$ ($ZT \sim 0.35$ at 630 K),^[18] germanite derivative $\text{Cu}_{22}\text{Fe}_8\text{Ge}_4\text{S}_{32}$ ($ZT \sim 0.17$ at 575 K)^[19]... Nevertheless, only few *n*-type sulfide thermoelectrics with moderate figure of merit are available, like Bi_2S_3 ($ZT \sim 0.6$ at 675 K),^[20–22] TiS_2 ($ZT \sim 0.5$ at 700 K),^[23–25] CuFeS_2 ($ZT \sim 0.21$ at 573 K),^[26] $\text{Cu}_4\text{Sn}_7\text{S}_{16}$ ($ZT \sim 0.21$ at 600 K),^[27] $\text{Cu}_2\text{CoTi}_3\text{S}_8$ ($ZT \sim 0.2$ at 670 K)^[28,29] and CuFe_2S_3 ($ZT \sim 0.14$ at 700 K).^[30] Very recently, Rathore *et al.* obtained a $ZT \sim 0.7$ at 820 K in the AgBiS_2 phase^[31] while Tan *et al.* reported an ultralow thermal conductivity and high $ZT \sim 1$ at 800 K for complex material AgBi_3S_5 doped with Cl.^[32] In such compound, Skoug and Morelli evidenced the relationship between the lone pair electrons of Bi^{3+} and the low thermal conductivity.^[33] In this context, we decided to prospect derivative Ag-free materials with complex unit cells and structural features which can induce strong phonon scattering.

The MnBi_4S_7 and FeBi_4S_7 are two isostructural ternary compounds, characterized by a complex layered crystal structure presenting structural similarities and same crystal symmetry as AgBi_3S_5 . Despite FeBi_4S_7 was discovered in 1972 by Sugaki *et al.*^[34], its crystal structure remained unresolved until Luo *et al.*'s work in 2013,^[35] which also described the first synthesis of the new MnBi_4S_7 phase and reported on the antiferromagnetic properties of the two compounds ($T_N = 31$

K and 67 K for MnBi₄S₇ and FeBi₄S₇, respectively). Yet, the other physical properties were not investigated and, regardless of their structural complexity, favorable to a low lattice thermal conductivity, these phases have not been further studied and their thermoelectric performances are still unknown.

In this article, we present for the first time a comprehensive study of the electrical and thermal properties behaviors of the XBi₄S₇ (X = Mn, Fe) phases above room temperature. Chemical bonding in these compounds is analyzed using quantum chemical calculations. As indicated by density functional theory (DFT) calculations, the multiple conduction bands observed in the electronic structure of XBi₄S₇ (X = Mn, Fe) compounds are responsible for the moderately high power factor of 0.2 mW m⁻¹ K⁻² at 700 K. Meanwhile, the thermal conductivity of polycrystalline samples of these materials is ultralow and ranges from 1 to 0.65 W m⁻¹ K⁻¹ from 300 to 700 K, respectively. This low thermal conductivity is ascribed to high the small Young's modulus, high Grüneisen parameter, and low Debye temperature. Overall, a thermoelectric figure of merit *ZT* of 0.21 (700 K) and 0.19 (600 K) is reached for MnBi₄S₇ and FeBi₄S₇, respectively. These results unveil the strong potential of MnBi₄S₇ as an efficient and affordable *n*-type thermoelectric material, as the *ZT* of undoped sample already reaches the performances of optimized *n*-type ternary and quaternary copper sulfides.

2. Experimental Section

The two compounds XBi₄S₇ (X = Mn, Fe) were synthesized from stoichiometric mixtures of Bi (>99.99%, Alfa Aesar), S (>99%, < 325 mesh, Alfa Aesar) and either Mn (>99.95%, < 325 mesh, Alfa Aesar) or Fe (>99%, < 200 mesh, Alfa Aesar). Bi needles were milled in a 45 mL tungsten carbide jar by means of a Pulverisette 7 Premium line (Fritsch) to obtain a < 200 μm powder. All the experiments were carried in an argon-filled glovebox to ensure an inert atmosphere during the synthesis. The precursors were weighed, thoroughly hand mixed in an agate mortar and loaded into silica tubes. The tubes were flame-sealed under primary vacuum and successively

heated at 100 K per hour up to 973 K (MnBi₄S₇) or 923 K (FeBi₄S₇) for 60 hours. Finally, the tubes were air-quenched in order to obtain single phase samples. Indeed, due to the metastable nature of these two phases,^[34] a gradual cooling ineluctably results in the presence of multiple phases in the samples with a high proportion of Bi₂S₃. The air-quenched samples were then grinded, loaded in 10 mm graphite dies and subsequently densified under vacuum by Spark Plasma Sintering (SPS) at 923 K for 25 min with a uniaxial pressure of 64 MPa. The heating and cooling rates were set to 100 K min⁻¹. Relative densities close to 95.8 % (MnBi₄S₇) and 97.2 % (FeBi₄S₇) of the theoretical values were obtained.

Synchrotron powder X-ray diffraction (PXRD) data were collected at the beamline CRISTAL (synchrotron SOLEIL, Saint Aubin, France). Acquisition were performed on powder loaded into a borosilicate glass capillary at energy of 21.312 keV ($\lambda = 0.5817 \text{ \AA}$) using a two-circle diffractometer equipped with a Mythen detector bank composed of 9 elements covering an angular range of $\sim 50^\circ$.^[36] Final diffraction patterns were obtained by the average of data acquired by the 9 elements during a non-continuous scan of 120° counting 3 s for each step of 1° . In order to maintain the same statistical significance for all the regions of the pattern, the initial and ending scan regions that have not been collected by all the 9 detector have been excluded from the average.

Powder neutron diffraction (PND) data were collected on D2B high-resolution two-axis diffractometer located at the Institut Laue-Langevin (Grenoble, France). The beamline was set up to its optimal wavelength of 1.5945 \AA using the [335] reflection of the multocrystal Ge[115] monochromator. The beamline is equipped by pseudo 2D high resolution positive sensitive detector composed by 128 element, covering a covering an angular range of $\sim 50^\circ$ with an angular resolution of 0.05° .^[37] The measurements were carried out on powders obtained by grinding the densified final samples ($\sim 3\text{g}$) loaded into cylinder vanadium sample holders. A complete diffraction pattern on the 2θ range $[5 - 165]^\circ$ was recorded by a 20 min acquisition scan in which

each step integration time was adjusted to reach 600000 counts on monitor detector, in order to compensate any beam flux fluctuation. Such acquisition was repeated 10 times in order to improve statistics and then averaged to obtain the final data.

Diffraction patterns of standard powders (silicon (NIST 640c) for X-ray and NAC ($\text{Na}_2\text{Ca}_3\text{Al}_2\text{F}_{14}$) for neutron) were also recorded in order to refine the corresponding wavelengths and to determine the instrumental broadening of diffraction peaks. The angular dependence of the Full Width at Half Maximum (FWHM) of the diffraction peaks obtained from those latter was determined using the Caglioti's function ($\text{FWHM}(\theta) = (U \tan^2(\theta) + V \tan(\theta) + W)^{1/2}$ where U, V and W are to be refined).^[38] The resulting Lorentzian and Gaussian contributions to the FWHM of the diffraction peaks were used as instrumental parameters for the Rietveld refinements. High-resolution PXRD and PND were simultaneously used to provide, respectively, high resolution of lattice distortions through subtle peak splitting and sensitivity to the light elements in the structure such as sulfur. Compared to separate data refinement, the combined refinements of these complementary diffraction patterns allow to determine more accurately the crystal structure of both MnBi_4S_7 and FeBi_4S_7 compounds. Both datasets (PXRD and PND) have been processed at the same time considering a unique crystallographic structure. The full profile-fitting refinements were carried out using the Rietveld method, with the *Fullprof* and *WinPlotr* software packages.^[39,40] The shape of the diffraction peaks was corrected from both instrumental parts using the resolution functions previously determined, and then, modeled using a Thompson-Cox-Hastings pseudo-Voigt profile function.^[41] Zero-point shift and asymmetry parameters were systematically refined, and the background contributions of both datasets were estimated using a polynomial function of order 12. Finally, lattice parameters, fractional atomic coordinates, isotropic displacement parameters (*i.e.* Debye-Waller factors: B_{iso}), and site occupancies were varied in order to refine the crystal structure of the MnBi_4S_7 and FeBi_4S_7 compounds. It should be mentioned that, as bismuth is the heaviest element in both structures,

their site occupancies have been fixed for all of the refinements to provide higher accuracy of other element site occupancies together with isotropic displacement parameters. The obtained refined crystallographic parameters are gathered in the supplementary information (**Tables S1** and **S2**).

The microstructures and chemical compositions were examined by Scanning Electron Microscopy (SEM) associated with Energy-Dispersive X-ray spectroscopy (EDX) using a ZEISS Supra 55.

The measurements of the electrical resistivity (ρ) and of the Seebeck coefficient (S) were simultaneously carried out between room temperature (RT) and 673 K on bar-shaped samples ($3.0 \times 3.0 \times 8.0 \text{ mm}^3$) with the four-probe method in a ZEM-3 system (ULVAC-RIKO) under a partial helium pressure. The charge carrier concentrations ($n_H = 1/eR_H$), where e is the electronic charge) and mobilities were determined from Hall effect measurements at RT with the Van der Pauw method using a PPMS (Physical Properties Measurement System) device from Quantum Design. The measurements were performed on $3.0 \times 3.0 \times 0.3 \text{ mm}^3$ samples, with indium paste as contacts. The Hall coefficients were obtained from the linear fits of the Hall resistivity versus magnetic fields between -7 and 7 T. Finally, the thermal diffusivity (D) was determined by the laser flash method on square samples ($6.0 \times 6.0 \times 1.0 \text{ mm}^3$) in a LFA 457 from Netzsch under an argon atmosphere. The total thermal conductivity (κ) was calculated according to the equation $\kappa = D \times Cp \times \rho_m$, where Cp is the heat capacity (deduced from the Dulong-Petit's law) and ρ_m is the geometrical density of the bulk sample. All the electrical and thermal properties measurements were performed along the direction perpendicular to the compressive stress applied during the densification process. The measurements uncertainties are about 8 % for the electrical resistivity, 6 % for the Seebeck coefficient, 11 % for the thermal conductivity and 16 % for the figure of merit, ZT .^[42]

^{57}Fe Mössbauer spectroscopy was performed in transmission mode at 295 K on powdered FeBi_4S_7 sample using a constant acceleration spectrometer and ^{57}Co in Rh matrix as the source. Isomer shifts are reported relative to metallic iron at room temperature.

Spin-polarized band structure and average properties were computed with the DFT Vienna ab initio Simulations Package (VASP).^[43,44] The exchange–correlation energy was taken into account using the generalized gradient approximation (GGA) with the Perdew–Burke–Ernzerhof (PBE) functional.^[45] Because of the presence of localized d electrons, an additional Hubbard-like term was introduced for Mn and Fe. The simplified Dudarev approach was used with $U_{\text{eff}} = U - J = 2.7$ eV for Mn 3d orbital and 4 eV for Fe 3d orbital.^[46] Since the Bi atoms have fairly high atomic number and mass, the effect of spin-orbit coupling was included to elucidate realistic electronic structure. The energy cutoff in the calculations is 350 eV for both compounds. The electronic wave function was sampled with $3 \times 3 \times 3$ k-points in the first Brillouin zone using the Monkhorst-Pack method.^[47] Chemical bonding analyses of plane-wave data by Crystal Orbital Hamiltonian Population (COHP)^[48] were done using LOBSTER.^[49–51] Band-structures, density of states (DOS) and COHP curves were shifted so that the Fermi level lies at 0 eV.

Phonon calculation has been performed by using density function perturbation theory (DFPT) as implemented in the CASTEP code.^[52] Prior to these calculations, cell parameters and atomic positions were both relaxed using spin-polarized GGA calculations considering the same additional Hubbard-like term previously mentioned for Mn and Fe. During the geometry optimizations, a convergence threshold of $0.02 \text{ eV } \text{Å}^{-1}$ was used for the residual forces and 0.1 kbar for the pressure. The calculation were performed using a set of norm-conserving pseudopotentials with the PBEsol exchange-correlation functional.^[53] The cutoff energy for plane-waves was set to 400 eV. A $7 \times 7 \times 2$ k-point mesh was used to sample the Brillouin zone.

3. Results and discussion

3.1. Diffraction analysis and spin-polarized DFT calculations

The combined Rietveld refinements of PXRD and PND patterns of sintered MnBi_4S_7 and FeBi_4S_7 samples are illustrated in **Figure 1**. Both synchrotron diffraction patterns present peaks FWHM comparable to standard Silicon (NIST 640c) indicating the absence of extensive crystal defects and micrometric crystallite size for the two samples. In both samples, all the diffraction peaks can be indexed with the monoclinic $C2/m$ ($n^\circ 12$) space group and lattice parameters deduced from the Rietveld refinements, $a = 12.927(6) / 12.762(2) \text{ \AA}$, $b = 3.973(6) / 3.964(1) \text{ \AA}$, $c = 11.823(6) / 11.804(5) \text{ \AA}$, $\beta = 104.666(4) / 104.422(2)^\circ$ for MnBi_4S_7 and FeBi_4S_7 , respectively. These values are in good agreement with the ones determined on single crystals by Luo *et al.*^[35] and on polycrystalline FeBi_4S_7 sample by Sugaki *et al.*^[34] Rietveld refinements were performed using the standardized crystal structural data arising from the study of Luo *et al.*^[34] as starting values. As it can be noticed from these refinements, no extra peaks or intensity mismatch can be observed, therefore indicating that both MnBi_4S_7 and FeBi_4S_7 samples are highly pure.

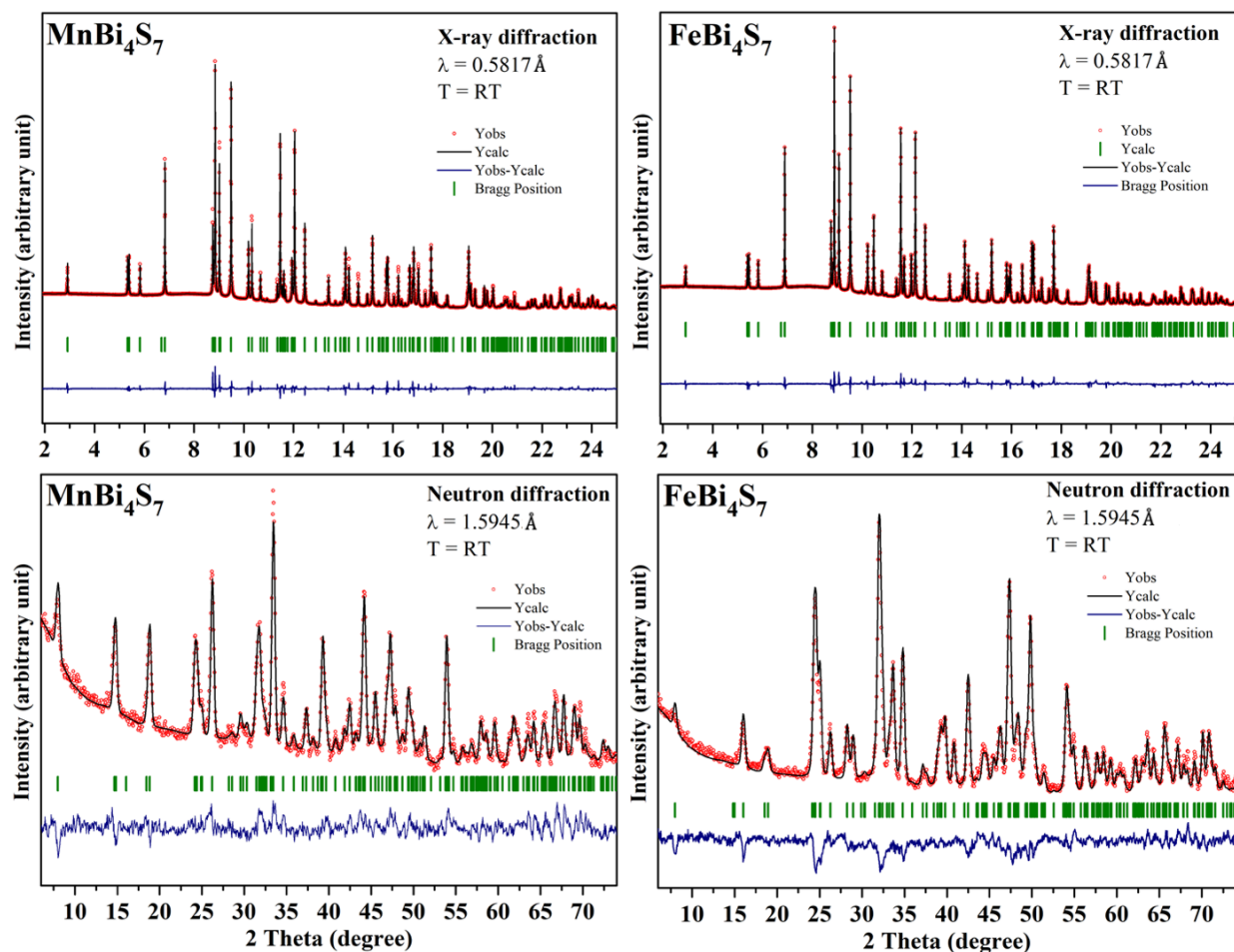


Figure 1. Rietveld refinements of PXRD (top) and PND patterns (bottom) of (left) MnBi_4S_7 and (right) FeBi_4S_7 sintered samples.

The crystallographic parameters deduced from the Rietveld refinements, such as reliability factors, atomic positions and bond lengths are gathered in **Tables S1** and **S2**. A schematic structure of XBi_4S_7 ($X = \text{Mn}, \text{Fe}$) compounds is displayed in **Figure 2a**. The crystal structure of both compounds, firstly described by Luo *et al.*,^[35] adopts the 2P structure of the pavonite homologous series.^[54,55] It may be depicted as a layered monoclinic structure (**Figure 2b**), composed of $[(\text{Mn},\text{Fe})\text{S}_6]$ octahedra chains along the two-fold axis surrounded on one side by $[\text{BiS}_6]$ octahedra chain and on the other side by distorted rectangular pyramidal $[\text{BiS}_5]$ chain. $[(\text{Mn},\text{Fe})\text{S}_6]$ octahedra shares apex with $[\text{BiS}_6]$ octahedra through S1 atom and edge with $[\text{BiS}_5]$

square pyramid through either two S3 atoms or one S1 and S3 atom (see **Figure 2a**). All Rietveld refinements were performed using two distinct crystallographic bismuth sites. The Bi1 (*4i* Wyckoff position) atom is located inside distorted octahedron formed by two S2 and two S4 atoms at 2.774(1) Å and 2.795(5) Å, respectively, forming a rectangular plane, and by one S2 atom at 2.739(9) Å and one S1 atom at 2.935(6) Å, respectively above and below this plane. Bi2 (also in *4i* Wyckoff position) atom is located inside distorted square pyramidal formed by two S1 and two S3 atoms at 2.704(7) Å and 3.039(4) Å, respectively, forming a rectangular plane and by one apical S3 atom at 2.608(4) Å. The coordination polyhedron of Bi2 atom is completed by two additional S2 atoms at longer distance of 3.377(1) Å. Thus, according to the bond character and strength, the Bi2 coordination polyhedron can also be considered as [BiS₃₊₂₊₂] type defined by Kupčik, with the two longest Bi-S distances indicating weak d bonds due to the activity of the lone pair.^[56] Finally, the Mn/Fe cations located in the *2d* Wyckoff position (0; ½; ½) are coordinated to six S atoms (S3 in a planar configuration and S1 located at the top and the bottom of the octahedron). The analysis of the (Mn,Fe)-S1 distances reveal a tetragonal distorted octahedron with longer distances in plane (2.721(3) Å and 2.714(7) Å for MnBi₄S₇ and FeBi₄S₇, respectively) than from the octahedron's apexes (2.478(5) Å and 2.470(8) Å for MnBi₄S₇ and FeBi₄S₇, respectively). It should be mentioned that our distances are quite similar to those obtained for both compounds by Luo *et al.* on single crystals.^[35] The good reliability factors combined with similar cell parameters and bond distances attest of the high crystallinity of both MnBi₄S₇ and FeBi₄S₇ samples.

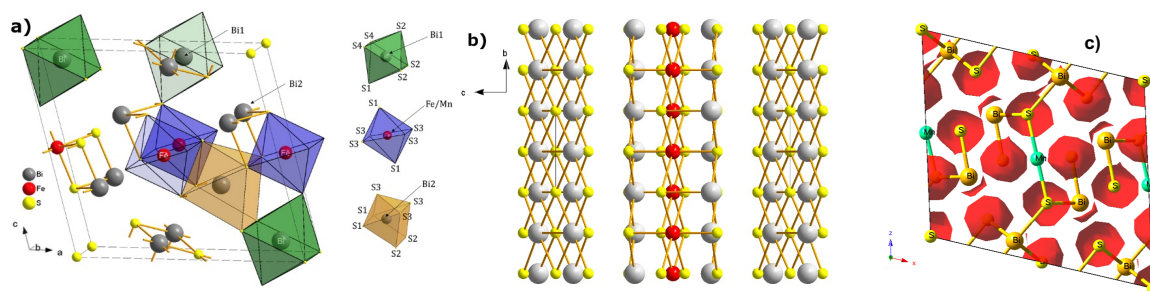


Figure 2. (a) Crystal structure of XBi_4S_7 ($X = \text{Mn, Fe}$) compounds with the coordination polyhedra of Mn/Fe, Bi1 and Bi2. (b) The projection along (100) highlights the layered structure of XBi_4S_7 phases. Grey, red and yellow spheres represent Bi, Mn/Fe and S atoms, respectively. (c) electron localization function (ELF) computed for MnBi_4S_7 .

Spin-polarized DFT calculations were carried out in order to have a better understanding of the chemical bonding and structural properties in both XBi_4S_7 compounds. Spin-polarized atom-projected and total DOS are sketched in **Figures 3** and **4** for MnBi_4S_7 and FeBi_4S_7 , respectively. Pristine compounds are both computed semiconducting with an optical band gap of 0.81 eV and 1.07 eV, respectively for MnBi_4S_7 and FeBi_4S_7 . These later values are in good agreement with experimental optical diffuse reflectance measurements and theoretical values previously reported in the literature.^[35] As magnetic properties are expected for these compounds, ferromagnetic states were computed. The computed cell moments for MnBi_4S_7 and FeBi_4S_7 compounds are equal to $5.38 \mu_{\text{B}}$ and $4.92 \mu_{\text{B}}$ per formula unit, respectively. These values are in a fair agreement with experimental ($5.67(4) \mu_{\text{B}}$ for MnBi_4S_7 and $4.60(1) \mu_{\text{B}}$ for FeBi_4S_7) previously determined by Luo *et al.*,^[35] as well as theoretical ones based on the spin-only magnetic moment expected for Mn^{2+} (d^5) and Fe^{2+} (d^6) ions both in high-spin configuration. It is noteworthy to mention that the ^{57}Fe Mössbauer spectrum of the FeBi_4S_7 compound at room temperature, shown in **Figure S1**, is consistent with Fe^{2+} ions in high-spin state.

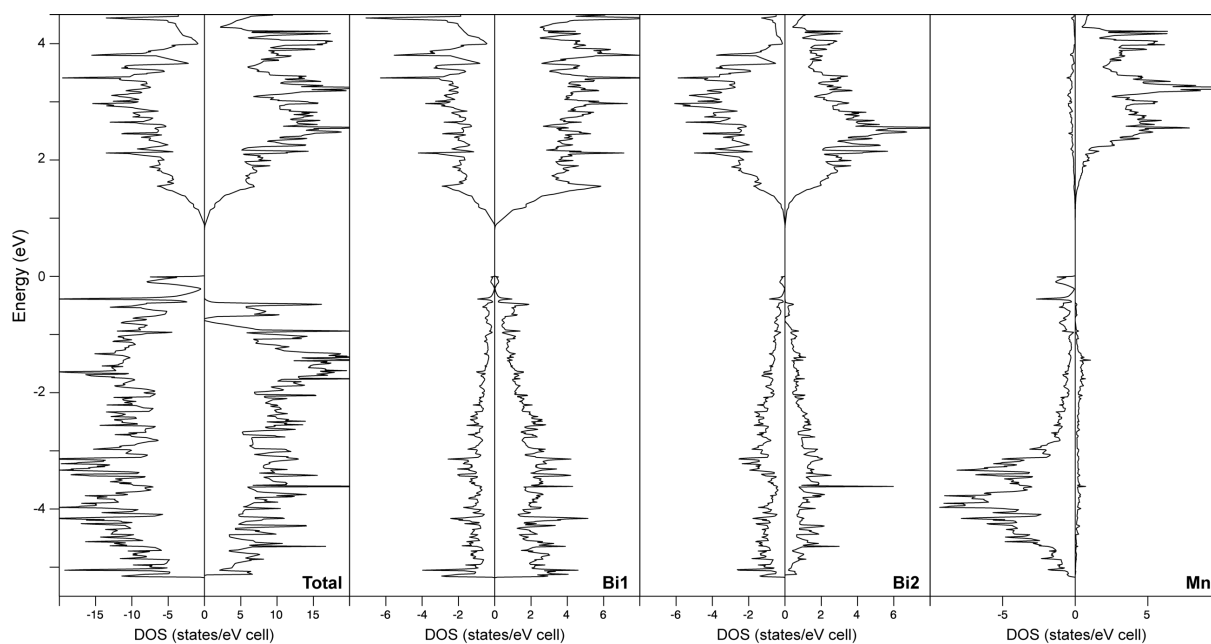


Figure 3. Spin-polarized total and atom projected density of states of MnBi_4S_7 phase.

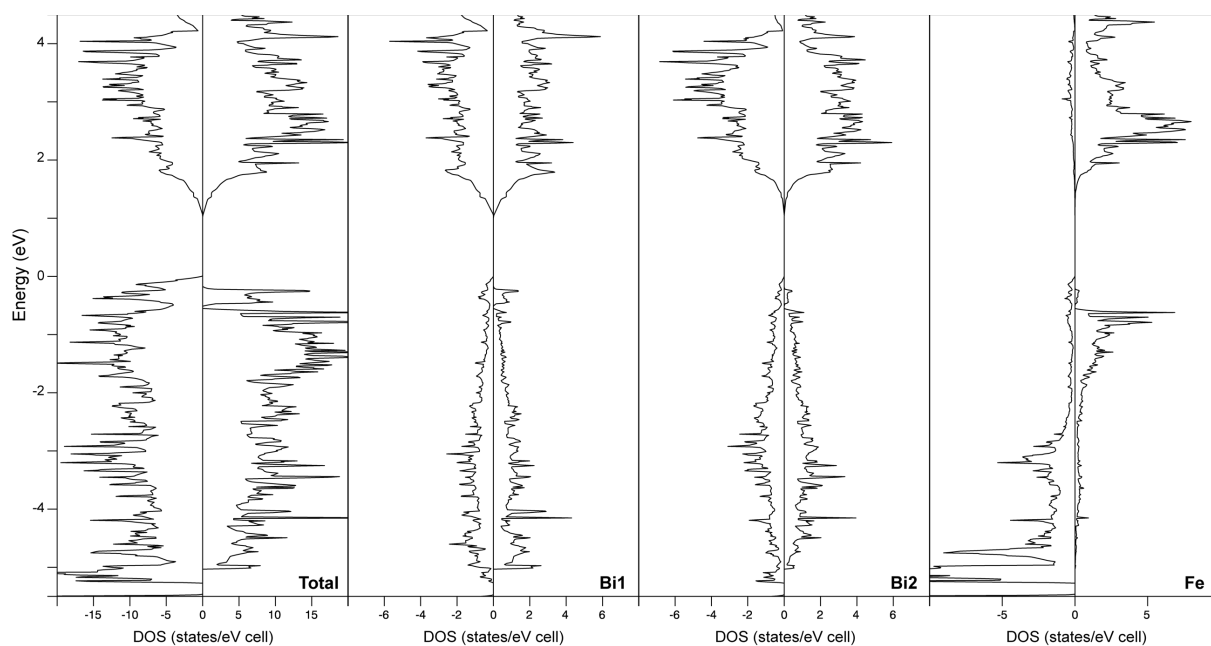
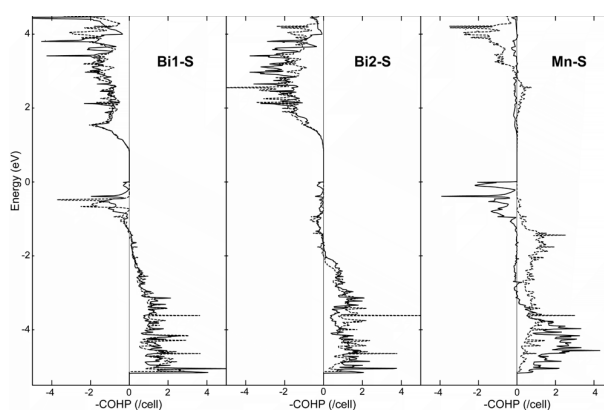


Figure 4. Spin-polarized total and atom projected density of states of FeBi_4S_7 phase.

The atom-projected DOS show that the bottom of the conduction band is mainly centered on Bi and S atoms in these compounds. Bi1-S, Bi2-S, and X-S (X = Mn, Fe) COHP curves are

displayed in **Figure 5**; they represent a measure of the magnitude of the bonding as they correspond to the Hamiltonian population-weighted DOS. For both compounds, the top of the valence band shows an antibonding Bi1-S character and an almost non-bonding Bi2-S character. The conduction bands are strongly Bi1-S and Bi2-S antibonding. Summing COHP values up to the Fermi level gives access to the contribution of a chemical bond to the distribution of one-particle energies and indicates the total bond strength. Such values are generally noted ICOHP; they are given in **Table 1** for Bi1-S, Bi2-S and X-S ($X = \text{Mn, Fe}$) contacts. Since Bi-S COHP curves for both spins hardly differ, up- and down-ICOHP values for these bonds are very close. Bi1-S bonds are computed stronger than Bi2-S bonds for both phases. This is consistent with longer distances with sulfur atoms for Bi2 compared to Bi1. The ICOHP values for X-S bonds strongly depend on the spin polarization, as expected from the strong magnetization of metal atoms in the structure. Fe-S bonds are computed weaker than Mn-S ones. For both compounds, the top of the spin-up valence band exhibits an antibonding X-S character (cf. **Figure 5**). Since Fe atoms have one additional valence electron compared to Mn, more X-S antibonding bands are occupied in FeBi_4S_7 than in Mn analogue.



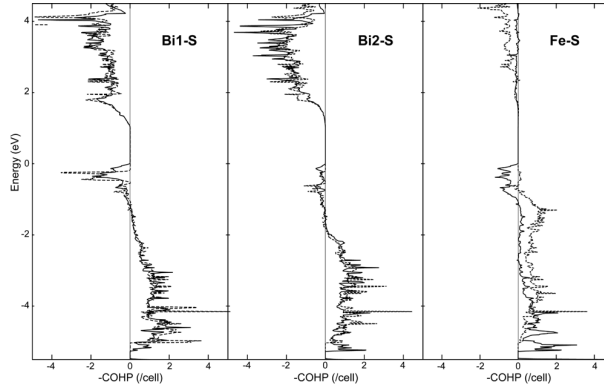


Figure 5. COHP curves for Bi1-S, Bi2-S and X-S (X = Mn, Fe) contacts computed for (top) MnBi_4S_7 and (bottom) FeBi_4S_7 compounds.

	Mn		Fe	
	up	down	up	down
Bi1-S	-6.47	-6.48	-6.59	-6.61
Bi2-S	-5.99	-6.01	-6.13	-6.14
X-S	-3.69	-4.89	-3.56	-4.77

Table 1. Spin-polarized ICOHP values (Ry/cell) for Bi1-S, Bi2-S, and X-S (X = Mn, Fe) contacts. ICOHP are summed for all the bonds of the coordination polyhedra sketched in **Figure 2a**.

The structural study has been completed with microstructural characterization by means of scanning electron microscopy (SEM). The SEM micrographs of the fractured cross-section of the densified samples are displayed in **Figure 6**. Both samples exhibit a dense microstructure with an anisotropic grain morphology which agrees with the layered structure of the XBi_4S_7 (X = Mn, Fe) phases. Moreover, EDX analyses reveal the presence of a small amount of Bi_2S_3

secondary phase in both samples (**Figure S2**). However, it should be pointed out that the amount of Bi_2S_3 is low for both samples and remains under the PXRD and PND detection limit.

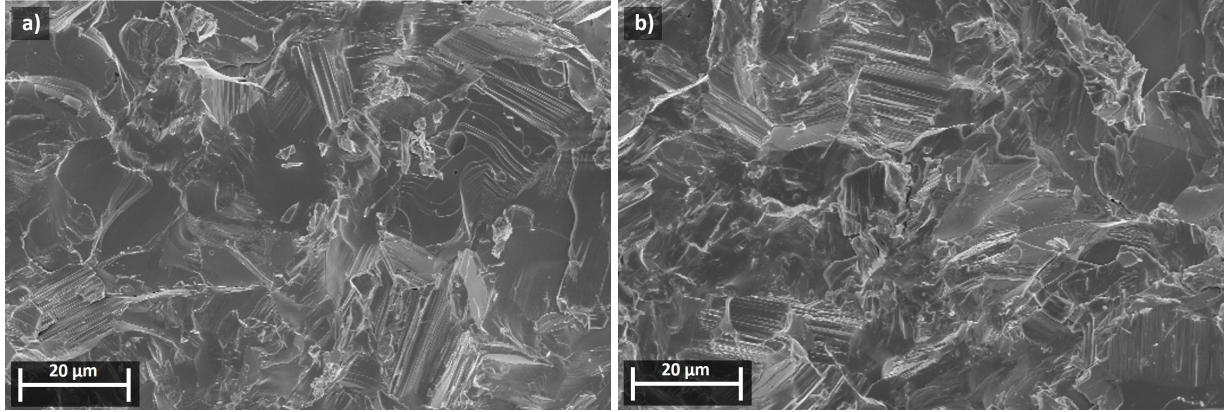


Figure 6. SEM micrographs of (a) MnBi_4S_7 and (b) FeBi_4S_7 sintered samples.

3.2. Electrical and thermal transport properties

Aiming to get further insight on the suitability of these phases for thermoelectric applications, the electrical resistivity, Seebeck coefficient and thermal conductivity have been measured. The electrical resistivity (ρ) of both phases as a function of the temperature is depicted in **Figure 7a**. The two samples reveal a metallic behavior with an increase of the electrical resistivity when the temperature rises. Both compounds exhibit slightly high electrical resistivity, with values of $5.3 \text{ m}\Omega \text{ cm}$ for MnBi_4S_7 and $7.1 \text{ m}\Omega \text{ cm}$ for FeBi_4S_7 at 300 K . The electrical resistivity of the two samples subsequently reaches $\sim 19 \text{ m}\Omega \text{ cm}$ at 700 K . It is noteworthy, that the temperature dependence of the electrical resistivity is not linear in the FeBi_4S_7 sample. This behavior seems to be linked with the low thermal stability of this compound as discussed in the next paragraph. With the purpose to determine the room temperature charge carrier concentrations (n_H) and mobilities (μ_H) of the samples, Hall effect measurements were performed. The negative Hall coefficients measured reveal that electrons are the major carriers in these two phases. The MnBi_4S_7 sample exhibits a room temperature carrier concentration close to $6.3 \times 10^{19} \text{ cm}^{-3}$ and

a mobility of $\sim 19 \text{ cm}^2 \text{ V}^{-1} \text{ s}^{-1}$ whereas the values for the FeBi_4S_7 sample are close to $5.7 \times 10^{19} \text{ cm}^{-3}$ and $\sim 16 \text{ cm}^2 \text{ V}^{-1} \text{ s}^{-1}$, respectively. Thus, the lower electrical resistivity in MnBi_4S_7 sample compared to FeBi_4S_7 is associated to a higher charge carrier concentration combined with a larger mobility. However, the difference of charge carrier concentration between the two phases is not so significant. As the synthesis of MnBi_4S_7 requested higher temperature (973 K) than for FeBi_4S_7 (923 K), the sulfur loss could be more pronounced in MnBi_4S_7 , creating electron doping. The **Figure 7b** displays the temperature dependence of the Seebeck coefficient (S) for the XBi_4S_7 samples ($X = \text{Mn}, \text{Fe}$). The negative values of the Seebeck coefficients confirm the n -type conductivity in these materials. It should be noted that these experimental results are opposite to the theoretical work of Azam *et al.* who predicted a p -type conductivity for both compounds.^[57] Nevertheless, the n -type character of XBi_4S_7 ($X = \text{Mn}, \text{Fe}$) phases was highly expected by analogy with Bi_2S_3 and AgBi_3S_5 compounds where sulfur vacancies are likely to occur and to provide electron doping. The value of the Seebeck coefficient decreases when the temperature raises, from $-87 \mu\text{V K}^{-1}$ and $-93 \mu\text{V K}^{-1}$ at 300 K to $-200 \mu\text{V K}^{-1}$ and $-191 \mu\text{V K}^{-1}$ at 700 K, for MnBi_4S_7 and FeBi_4S_7 , respectively.

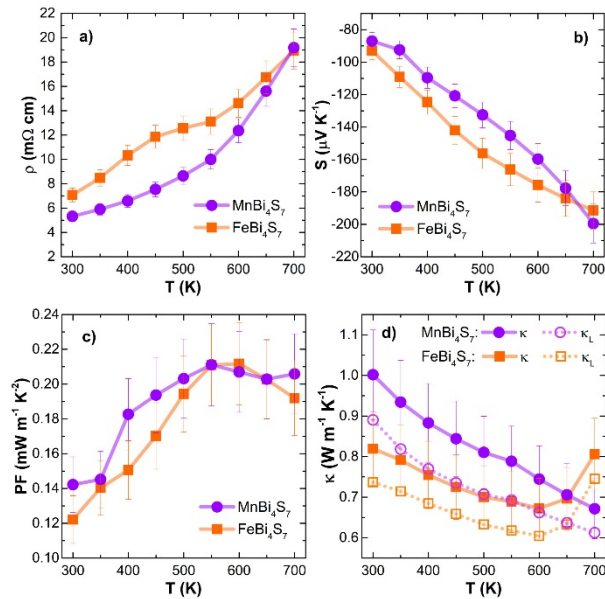


Figure 7. Temperature dependence of (a) electrical resistivity, (b) Seebeck coefficient, (c) power factor, and (d) thermal conductivity of the XBi_4S_7 ($\text{X} = \text{Mn}, \text{Fe}$) compounds.

Since these two phases are known as metastable, special attention has been devoted to assess the thermal stability of the compounds in the temperature range between 300 and 700 K. The electrical resistivity and Seebeck measurements were performed during several heat and cooling cycles. The results of the experiments are respectively illustrated in **Figures S3** and **S4**. While the MnBi_4S_7 phase has a good thermal stability below 700 K, the Fe analogue is not stable as clearly outlined by the large deviation of the electrical resistivity and Seebeck coefficient during the cycles. As shown in the PXR analysis performed after the cycling (**Figure S5**), this behavior is linked to the thermal decomposition of the FeBi_4S_7 phase to Bi_2S_3 .

The dependence of the Seebeck coefficients on carrier concentration is illustrated by the Pisarenko relation in **Figure 8**. The solid and dashed curves (MnBi_4S_7 and FeBi_4S_7 , respectively) were generated using single parabolic band (SPB) model with acoustic phonon scattering as the dominant scattering event.^[58,59] At 300 K, both samples are found to be well-fitted with Pisarenko curves, indicating that the description of the SPB model is valid for both materials in very good agreement with the band structure calculations discussed later (**Figure 9**). The room temperature calculation of the electron effective masses (m^*) of XBi_4S_7 ($\text{X} = \text{Mn}, \text{Fe}$) samples were respectively found to be close to $0.71 m_e$ and $0.72 m_e$. These values are significantly higher than the effective masses of AgBi_3S_5 ($0.22 m_e$)^[32] and Bi_2S_3 ($0.40 m_e$)^[60] and helps to maintain high Seebeck coefficient values despite the relatively large charge carrier concentration.

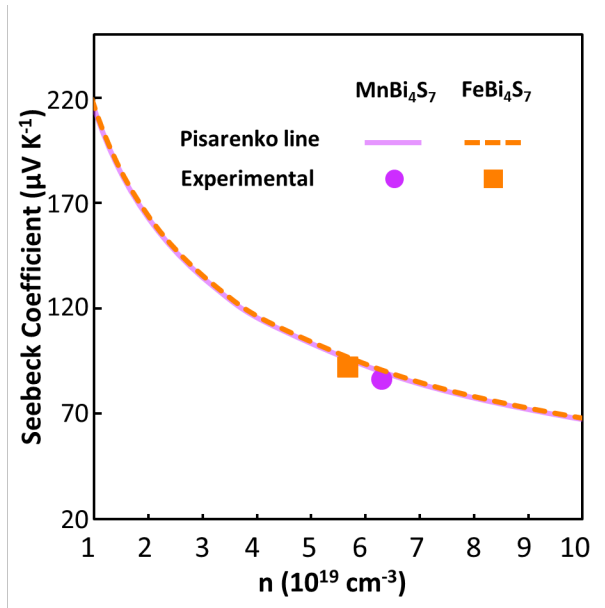


Figure 8. Absolute value of the Seebeck coefficient as a function of the Hall carrier concentration at room temperature, comparison of SPB model (lines) and experimental values (dots).

As shown in **Figure 7c**, the power factor ($PF = S^2/\rho$) of both phases gradually increases up to 550 K and reach approximately $0.21 \text{ mW m}^{-1} \text{ K}^{-2}$. The PF then slightly drops to $0.20 \text{ mW m}^{-1} \text{ K}^{-2}$ and $0.19 \text{ mW m}^{-1} \text{ K}^{-2}$ at 700 K for MnBi_4S_7 and FeBi_4S_7 , respectively, due to the increase of the electrical resistivity with the rising of the temperature.

In order to provide a deeper understanding of the transport properties of these two phases, DFT calculations were performed. Since vibrational properties have also been studied, the crystal structures of both compounds were geometry-optimized using PBEsol functional. This exchange-correlation functional is known to produce high-accuracy optimizations. Thus, the average discrepancy between theoretical and experimental structures is approximately 1%, as demonstrated in **Table S3**. The band structures sketched in **Figure 9** show that the two phases have an indirect band gap with the valence band maximum (VBM) and conduction band minimum (CBM) respectively located along $D \rightarrow Y$ line and at the C point of the first Brillouin zone. Furthermore, the **Figure 9** clearly highlights that the valence bands are multiple, and the energy gap between the first and fifth bands is less than 0.05 eV. This value is smaller than the

0.15 eV between the first and the second valence bands of PbTe.^[61,62] Although the band structure calculations for both compounds reveal multiple conduction bands near the conduction band minimum, they may not be sufficiently activated since the energy gap between the first and the fifth bands is slightly high (~0.2 eV). These later results indicate that the single parabolic band (SPB) can be expected as a valid model for both *n*-type compounds.

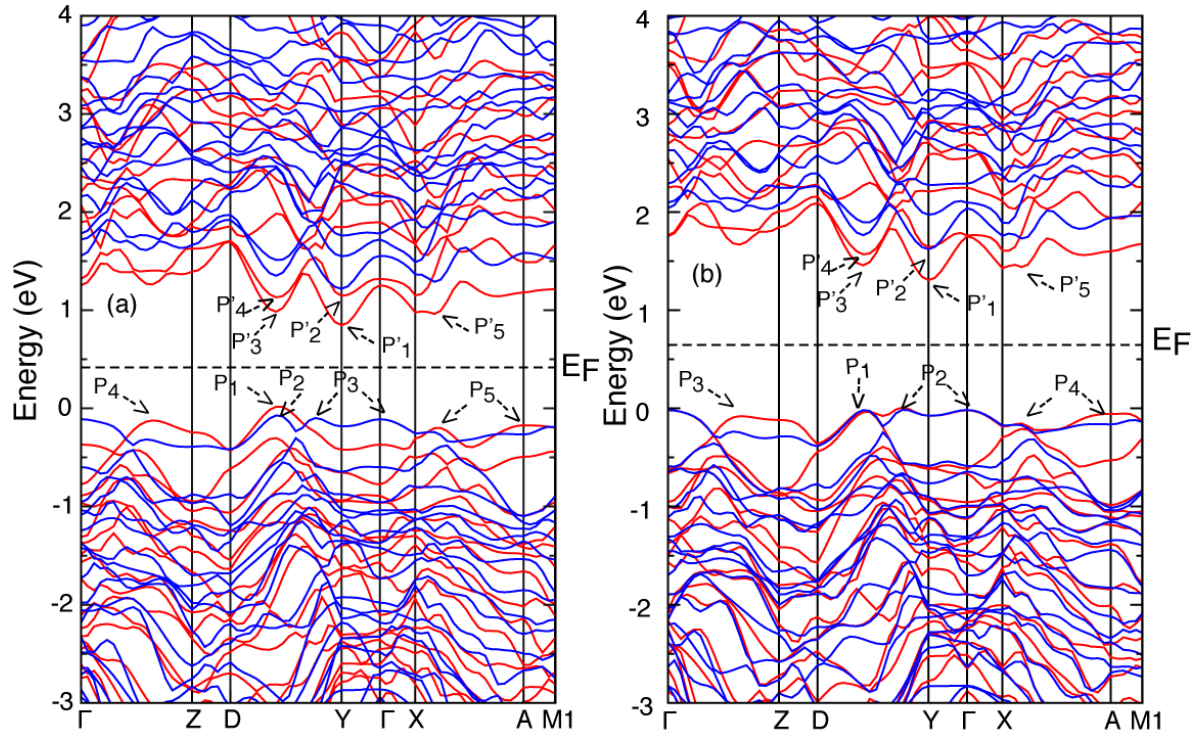


Figure 9. Spin-polarized band structure of (a) MnBi₄S₇ and (b) FeBi₄S₇. The red lines highlight spin up while the blue lines stand for spin down.

To conclude this study, the thermal conductivity (κ) of the samples has been determined between 300 K and 700 K (**Figure 7d**). Compared to MnBi₄S₇, the Fe derivative exhibits a lower thermal conductivity. At 300 K, the thermal conductivity of MnBi₄S₇ is close to 1 W m⁻¹ K⁻¹ while the value of the FeBi₄S₇ sample is around 0.82 W m⁻¹ K⁻¹. Both values gradually decrease upon

heating, respectively to a minimum of $0.67 \text{ W m}^{-1} \text{ K}^{-1}$ at 700 K for MnBi_4S_7 and $0.67 \text{ W m}^{-1} \text{ K}^{-1}$ at 600 K for FeBi_4S_7 . This value subsequently rises to $0.81 \text{ W m}^{-1} \text{ K}^{-1}$ at 700 K. This increase can be linked to the decomposition of FeBi_4S_7 to Bi_2S_3 as demonstrated by the PXRD performed on the sample after the diffusivity measurement (**Figure S6**). The total thermal conductivity (κ) results from the contributions of the lattice thermal conductivity (κ_L) and of the electronic thermal conductivity (κ_e) according to the relation: $\kappa = \kappa_L + \kappa_e$. In order to determine if the lower thermal conductivity of FeBi_4S_7 originates from the electronic or lattice contribution, the electronic thermal conductivity was obtained from the Wiedmann-Franz relation: $\kappa_e = LT\sigma$. The Lorenz number L was calculated as function of temperature from the experimental Seebeck coefficients using single parabolic band model.^[58] The estimated Lorenz numbers (**Figure S7**) are in the range of $1.98 \times 10^{-8} \text{ W } \Omega \text{ K}^{-2}$ and $1.63 \times 10^{-8} \text{ W } \Omega \text{ K}^{-2}$, which are lower than the metallic limit of $2.45 \times 10^{-8} \text{ W } \Omega \text{ K}^{-2}$.^[63] As displayed in **Figure S8**, the resulting electronic thermal conductivity is around $0.11 \text{ W m}^{-1} \text{ K}^{-1}$ and $0.08 \text{ W m}^{-1} \text{ K}^{-1}$ at 300 K for MnBi_4S_7 and FeBi_4S_7 , respectively, and decreases to $0.06 \text{ W m}^{-1} \text{ K}^{-1}$ at 700 K. Thus, the difference of the electronic thermal conductivity is not significant enough to support the difference between the total thermal conductivity of the two samples. Thereby, the gap between the two compounds comes from a difference of the lattice thermal conductivity, as illustrated in **Figure 7d**. According to the first-principles calculations, Bi-S and X-S (X = Mn, Fe) bonds are stronger in MnBi_4S_7 than in the Fe analogue. This theoretical result is experimentally supported by the lower lattice thermal conductivity of FeBi_4S_7 compared to MnBi_4S_7 . Softer bonds in the Fe compounds may be at the origin of its lower thermal conductivity. The intrinsically low thermal conductivity ($\kappa \sim 0.67 \text{ W m}^{-1} \text{ K}^{-1}$ at 600K) of both XBi_4S_7 (X = Mn, Fe) compounds is comparable to those of other materials, such as AgSbTe_2 ($\kappa \sim 0.73 \text{ W m}^{-1} \text{ K}^{-1}$ at 600 K)^[64,65] Ag_9TlTe_5 ($\kappa \sim 0.27 \text{ W m}^{-1} \text{ K}^{-1}$ at 600K),^[66] BiCuOSe ($\kappa \sim 0.45 \text{ W m}^{-1} \text{ K}^{-1}$ at 600K),^[67-70] $\text{K}_2\text{Bi}_8\text{Se}_{13}$ ($\kappa \sim 0.43 \text{ W m}^{-1} \text{ K}^{-1}$ at 600K),^[71] $\text{Ag}_4\text{Mo}_9\text{Se}_{11}$ ($\kappa \sim 0.73 \text{ W m}^{-1} \text{ K}^{-1}$ at 600K).^[72]

Aiming to further elucidate the origin of the low thermal conductivity of these two systems, the longitudinal (v_l) and transversal (v_t) phonon velocities, Young's moduli (E), Grüneisen parameters (γ) and Debye temperatures were computed for both phases from phonon and elastic properties calculations (**Table 2**). The Grüneisen parameter (γ) represents a measure of the bonding anharmonicity and governs the phonon–phonon scattering rate.^[64] Thus, a large Grüneisen parameter and a low Young's modulus often lead to a low thermal conductivity.

Table 2. Calculated longitudinal (v_l), transverse (v_t), and average (v_m) sound velocities, Poisson ratio (ν_p), Young's modulus (E), Grüneisen parameter (γ) and Debye temperature (θ_D) for the XBi_4S_7 ($X = \text{Mn, Fe}$) phases.

	v_l (m s^{-1})	v_t (m s^{-1})	v_m (m s^{-1})	ν_p	E (GPa)	γ	θ_D (K)
MnBi₄S₇	2537	1607	1767	0.18	39.9	1.16	179.4
FeBi₄S₇	2907	1782	1967	0.21	28.5	1.28	200.8

The mean sound velocity of both compounds $\text{MnBi}_4\text{S}_7/\text{FeBi}_4\text{S}_7$ (1767/1967 m s^{-1}) are comparable to those of $\text{K}_2\text{Bi}_8\text{Se}_{13}$ (1607 m s^{-1}),^[71] AgSbTe_2 (1727 m s^{-1}),^[64] BiSbSe_3 (1629 m s^{-1}),^[73] Bi_2Se_3 (2083 m s^{-1}),^[74] and BiCuOS/Se (2126/2107 m s^{-1})^[69,75] which have low thermal conductivity. Furthermore, the Young's moduli are close to 39.9 GPa and 28.5 GPa for MnBi_4S_7 and FeBi_4S_7 , respectively. These values are consistent with the chemical bonding analysis based on the calculations of COHP (*vide supra*). They are comparable to the ones of AgSbTe_2 ($E=39.2$ GPa),^[64] $\text{K}_2\text{Bi}_8\text{Se}_{13}$ ($E=37.1$ GPa)^[71] or BiSbSe_3 ($E=34.9$ GPa)^[73] and even lower than the values obtained in BiCuOSe ($E=76.5$ GPa)^[70] and Bi_2Se_3 ($E=70.3$ GPa)^[74] compounds. Generally, a low Young's modulus material is considered to have 'soft' bonding and consequently a slow

transport of phonons, resulting in a low lattice thermal conductivity. The Grüneisen parameters (γ) were calculated to be equal to 1.16 and 1.28 for MnBi_4S_7 and FeBi_4S_7 phases, respectively. Large values are generally indicative of strong anharmonicity and phonon scattering. These values are close to those computed for PbTe (1.45), AgSbTe_2 (2.05), BiSbSe_3 (1.89) and $\text{Ag}_2\text{Tl}_2\text{Mo}_9\text{Se}_{11}$ (0.9) which exhibit thermal conductivity at RT close to 2.4, 0.68, 0.59 and 0.6 $\text{W m}^{-1} \text{K}^{-1}$, respectively.^[64,73,76,77]

The small Young's moduli, high Grüneisen parameters and low thermal conductivity of both compounds are believed to be partly derived from the Bi^{3+} lone pair electrons. As described in the crystal structure section, the structure has two types of Bi atoms with different coordination environments. This leads to low crystal symmetry and several types of distorted polyhedra varying from octahedral $[\text{BiS}_6]$ to bicapped trigonal prism $[\text{BiS}_{3+2+2}]$. The optimized Bi-S bonds in the polyhedra vary greatly from 2.60 Å to 3.37/3.36 Å for $\text{MnBi}_4\text{S}_7/\text{FeBi}_4\text{S}_7$ compounds, respectively. The distortions in the Bi2 coordination polyhedra indicate that the electron lone pair of Bi^{3+} ($6s^2$) is stereochemically active and occupy its own space, in agreement with DFT electron localization function (ELF) shown in **Figure 2c**. Furthermore, Bi1 atoms are more strongly bonded to S atoms than Bi2 atoms according to ICOHP values (cf. **Table 1**). These distortions of the crystal lattice induce highly anharmonic behavior and consequently a large Grüneisen parameter. Similar results have been recently found in Bi/Sb containing complex materials as AgBiS_2 ,^[31] AgBi_3S_5 ,^[32] AgSbSe_2 ,^[78] $\text{Cu}_{12}\text{Sb}_4\text{S}_{13}$,^[79] $\text{K}_2\text{Bi}_8\text{Se}_{13}$,^[71] and Sb_2Se_3 .^[80]

The value of the Debye temperature θ_D also reflects the thermal conductivity and is defined as follows:^[81]

$$\theta_D = \frac{h}{k_B} \left(\frac{3N}{4\pi V} \right)^{1/3} v_m \quad (1)$$

where h is Planck's constant, k_B is the Boltzmann's constant, N is the number of atoms in a unit cell, V is the unit-cell volume. Through the equation 1, the Debye temperatures of MnBi_4S_7 and FeBi_4S_7 were respectively estimated to ~ 180 K and ~ 200 K. These values are slightly low compared with Bi_2Se_3 (~ 205 K)^[74] and BiCuOSe (~ 243 K),^[70] and in good agreement with the low thermal conductivity in these systems. Assuming that the heat is conducted only by acoustic phonons via Umklapp or/and normal scattering processes, the thermal conductivity can be computed by Slack's equation.^[82]

The thermal conductivity is calculated to be close to $0.72 \text{ W m}^{-1} \text{ K}^{-1}$ and $0.83 \text{ W m}^{-1} \text{ K}^{-1}$ at 600 K for MnBi_4S_7 and FeBi_4S_7 compounds, respectively. Our estimated values are slightly higher than the experimental observations, previously discussed with the **Figure 7d**. This discrepancy suggests that the effect of optical-acoustic phonon scattering should not be ignored. The optical-phonon scattering is expected because of the presence of heavy elements such as Bi which is supposed to have softer optical modes. In order to clarify this point, the phonon dispersion calculation in function of Brillouin zone around Γ point direction has been performed (**Figure 10**). Although phonon calculations within the harmonic approximation do not provide direct information on the thermal conductivity, the phonon dispersions show compressed acoustic branches which lead to low heat carrier velocity and low thermal conductivity.^[32,83] Moreover, the presence of low frequencies optic modes (22 and 45 cm^{-1}) that can interact with the acoustic vibration modes is known to introduce scattering channels that affect the thermal conductivity.^[84,85] This conjecture agrees with the observations in BiCuOS and skutterudites materials that have very low thermal conductivities.^[84,86–88] Finally, the theoretical minimum thermal conductivity κ_{min} was computed using the shortest scattering distance within the model proposed by Cahill *et al.*^[89] The resulting values are close to $0.37 \text{ W m}^{-1} \text{ K}^{-1}$ and $0.42 \text{ W m}^{-1} \text{ K}^{-1}$ for MnBi_4S_7 and FeBi_4S_7 phases, respectively. For both samples, the κ_L values are significantly higher than the κ_{min} values, indicating that further reduction might be achieved, for instance, by

reducing the grain size to enhance the boundary scattering of heat-carrying phonons or by enhancing structural disordering.^[90–94]

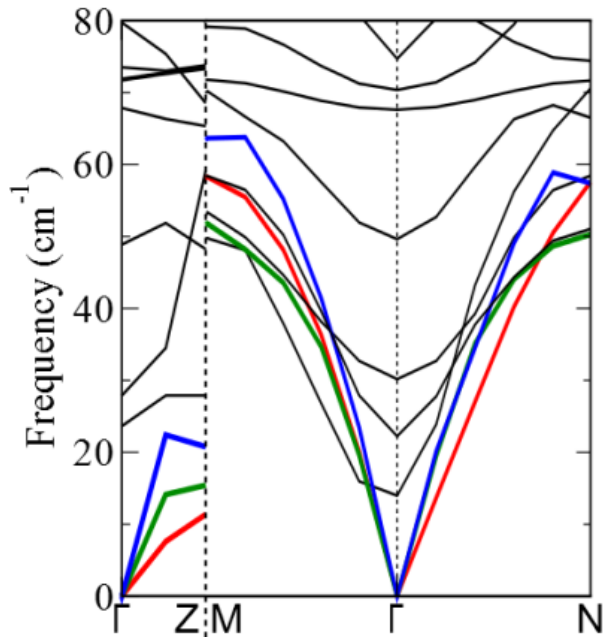


Figure 10. Phonon dispersion of MnBi₄S₇ around the Γ point. The black lines highlight the optical modes while the red, green and blue lines stand for transverse (TA/TA') and longitudinal (LA) acoustic modes, respectively.

In the end, the temperature dependence of the figure of merit (ZT) for the XBi₄S₇ ($X = \text{Mn, Fe}$) phases can be deduced by combination of electrical and thermal transport properties (**Figure 11**). Thanks to a moderate power factor combined with an intrinsically low thermal conductivity, the ZT of MnBi₄S₇ reaches 0.21 at 700 K. Despite this auspicious result, the Fe analogue seems less interesting for potential thermoelectric applications. Indeed, the ZT of FeBi₄S₇ peaks around 0.19 at 600 K and decreases for higher temperatures. This decline is attributed to the decomposition of FeBi₄S₇ as discussed earlier, which indicates the low stability of this phase and precludes its use as thermoelectric materials for medium temperature application. Even so, it is noteworthy that MnBi₄S₇ is stable up to 700 K.

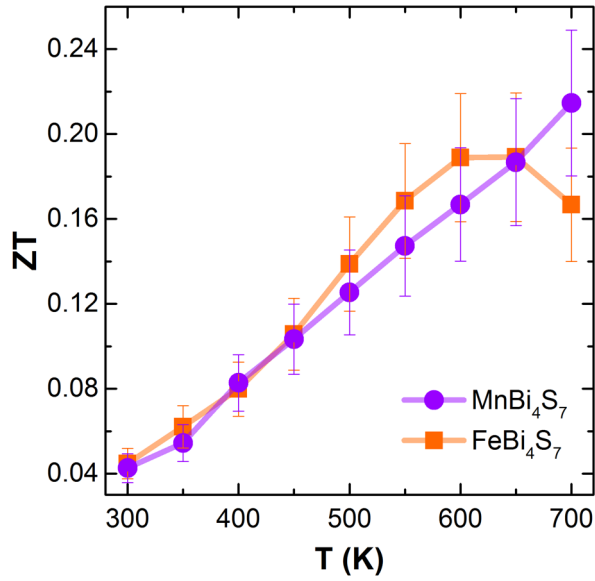


Figure 11. Temperature dependence of the thermoelectric figure of merit (ZT) of the XBi_4S_7 ($X = Mn, Fe$) compounds.

4. Conclusion

In this study, the investigation of the thermoelectric performances of the XBi_4S_7 ($X = Mn, Fe$) phases has been performed. The combination of experimental and theoretical results highlights the promising performances of the $MnBi_4S_7$ compound, while $FeBi_4S_7$ decomposes above approximately 600 K. Low lattice thermal conductivities of $0.9\text{-}0.6 \text{ W m}^{-1} \text{ K}^{-1}$ were observed in the temperature ranges from 300 to 700 K. Direct phonon velocity, elastic and phonon calculations suggest that low thermal conductivities stem from the small Young's modulus, high Grüneisen parameter, and low Debye temperature, which are related to its complex low symmetry monoclinic crystal structure. The difference between $MnBi_4S_7$ and $FeBi_4S_7$ may originate from differences in the chemical bonding in these compounds: Bi-S and X-S ($X = Mn$ or Fe) bonds are stronger in the Mn compound since less antibonding bands are occupied in this latter compared to Fe analogue. The combination of the power factor and low thermal

conductivity leads to a relatively high ZT value of 0.21 at 700 K for the MnBi_4S_7 phase without any optimizations. Thus, this figure of merit rises at the same level as undoped AgBi_3S_5 and state-of-the-art n -type ternary and quaternary copper sulfides. Furthermore, the extensive thermal properties calculations emphasize that the lattice thermal conductivity could reach even lower values with appropriate tuning of the microstructure. Several other strategies could also be used to lower the electrical resistivity and increase the power factor. In that respect, the control of sulfur vacancies and the substitution of sulfur by halogens were already revealed as relevant approaches to substantially improve the ZT of related sulfide compounds.

Supporting Information

The Supporting Information is available free of charge on the ACS Publications website at DOI :

Figure S1. ^{57}Fe Mössbauer spectrum of FeBi_4S_7 sintered compound at room temperature.

Figure S2. SEM with backscattered electrons and EDX analyses of the XBi_4S_7 ($\text{X} = \text{Mn}, \text{Fe}$) samples.

Figure S3. Evolution of the electrical resistivity of the MnBi_4S_7 and FeBi_4S_7 samples during cycling between 300 K and 700 K.

Figure S4. Evolution of the Seebeck coefficient of the MnBi_4S_7 and FeBi_4S_7 samples during cycling between 300 K and 700 K.

Figure S5. PXRD pattern of FeBi_4S_7 sample before and after the cycling in the 300 K to 700 K range.

Figure S6. PXRD pattern of FeBi_4S_7 sample before and after the Laser Flash Analysis at 700 K.

Figure S7. Lorenz number as a function of temperature for the XBi_4S_7 ($\text{X} = \text{Mn}, \text{Fe}$) samples.

Figure S8. Electronic thermal conductivity as a function of temperature for the XBi_4S_7 ($\text{X} = \text{Mn}, \text{Fe}$) samples.

Table S1. Structural parameters determined from combined PXRD/PND data Rietveld refinements of MnBi₄S₇ sample.

Table S2. Structural parameters determined from combined PXRD/PND data Rietveld refinements of FeBi₄S₇ sample.

Table S3. Comparison of experimental and theoretical lattice parameters.

Table S4. Calculated single crystal elastic constants, bulk moduli and compressibility coefficients of XBi₄S₇ (X = Mn, Fe) compounds.

Author Information

Corresponding Authors

E-mail: emmanuel.guilmeau@ensicaen.fr. Tel: +33 231 45 13 67.

E-mail: rabih.orabi@solvay.com. Tel: +33 428 27 10 80.

† J.-B. Labégorre and A. Virfeu contributed equally to this work.

Acknowledgements

The authors would like to thank Jérôme Lecourt and Christelle Bilot for technical support and Solvay Chemical compangny for financial support. The authors are indebted to the Institut Laue Langevin, Grenoble, France (<https://doi.ill.fr/10.5291/ILL-DATA.5-21-1112>) and synchrotron SOLEIL, Saint-Aubin, France (CRISTAL beamline, proposal 20181273) for the provision of research facilities.

References

- [1] D. M. Rowe, *Thermoelectrics Handbook: Macro to Nano*; CRC Press: Boca Raton, FL, 2006.

- [2] K. Suekuni, K. Tsuruta, T. Ariga, M. Koyano, *Appl. Phys. Express* **2012**, *5*, 051201.
- [3] K. Suekuni, K. Tsuruta, M. Kunii, H. Nishiate, E. Nishibori, S. Maki, M. Ohta, A. Yamamoto, M. Koyano, *J. Appl. Phys.* **2013**, *113*, 043712.
- [4] X. Lu, D. T. Morelli, Y. Xia, F. Zhou, V. Ozolins, H. Chi, X. Zhou, C. Uher, *Adv. Energy Mater.* **2013**, *3*, 342.
- [5] T. Barbier, P. Lemoine, S. Gascoin, O. I. Lebedev, A. Kaltzoglou, P. Vaqueiro, A. V. Powell, R. I. Smith, E. Guilmeau, *J. Alloys Compd.* **2015**, *634*, 253.
- [6] T. Barbier, S. Rollin-Martinet, P. Lemoine, F. Gascoin, A. Kaltzoglou, P. Vaqueiro, A. V. Powell, E. Guilmeau, *J. Am. Ceram. Soc.* **2016**, *99*, 51.
- [7] K. Suekuni, F. S. Kim, H. Nishiate, M. Ohta, H. I. Tanaka, T. Takabatake, *Appl. Phys. Lett.* **2014**, *105*, 132107.
- [8] K. Suekuni, F. S. Kim, T. Takabatake, *J. Appl. Phys.* **2014**, *116*, 063706.
- [9] C. Bourgès, Y. Bouyrie, A. R. Supka, R. Al Rahal Al Orabi, P. Lemoine, O. I. Lebedev, M. Ohta, K. Suekuni, V. Nassif, V. Hardy, R. Daou, Y. Miyazaki, M. Fornari, E. Guilmeau, *J. Am. Chem. Soc.* **2018**, *140*, 2186.
- [10] V. Pavan Kumar, A. R. Supka, P. Lemoine, O. I. Lebedev, B. Raveau, K. Suekuni, V. Nassif, R. Al Rahal Al Orabi, M. Fornari, E. Guilmeau, *Adv. Energy Mater.* **2019**, *9*, 1803249.
- [11] Y. Shen, C. Li, R. Huang, R. Tian, Y. Ye, L. Pan, K. Koumoto, R. Zhang, C. Wan, Y. Wang, *Sci. Rep.* **2016**, *6*, 32501.
- [12] H. Zhao, X. Xu, C. Li, R. Tian, R. Zhang, R. Huang, Y. Lyu, D. Li, X. Hu, L. Pan, Y. Wang, *J. Mater. Chem. A* **2017**, *5*, 23267.
- [13] P. Qiu, T. Zhang, Y. Qiu, X. Shi, L. Chen, *Energy Environ. Sci.* **2014**, *7*, 4000.
- [14] G. Guélou, A. V. Powell, P. Vaqueiro, *J. Mater. Chem. C* **2015**, *3*, 10624.
- [15] V. Pavan Kumar, T. Barbier, P. Lemoine, B. Raveau, V. Nassif, E. Guilmeau, *Dalt. Trans.* **2017**, *46*, 2174.
- [16] S. O. J. Long, A. V. Powell, P. Vaqueiro, S. Hull, *Chem. Mater.* **2018**, *30*, 456.

- [17] M.-L. Liu, F.-Q. Huang, L.-D. Chen, I.-W. Chen, *Appl. Phys. Lett.* **2009**, *94*, 202103.
- [18] V. Pavan Kumar, T. Barbier, V. Caignaert, B. Raveau, R. Daou, B. Malaman, G. Le Caër, P. Lemoine, E. Guilmeau, *J. Phys. Chem. C* **2017**, *121*, 16454.
- [19] V. Pavan Kumar, L. Paradis-Fortin, P. Lemoine, V. Caignaert, B. Raveau, B. Malaman, G. Le Caër, S. Cordier, E. Guilmeau, *Inorg. Chem.* **2017**, *56*, 13376.
- [20] K. Biswas, L.-D. Zhao, M. G. Kanatzidis, *Adv. Energy Mater.* **2012**, *2*, 634.
- [21] X. Du, F. Cai, X. Wang, *J. Alloys Compd.* **2014**, *587*, 6.
- [22] R. Chmielowski, D. Péré, C. Bera, I. Opahle, W. Xie, S. Jacob, F. Capet, P. Roussel, A. Weidenkaff, G. K. H. Madsen, G. Dennler, *J. Appl. Phys.* **2015**, *117*, 125103.
- [23] E. Guilmeau, Y. Bréard, A. Maignan, *Appl. Phys. Lett.* **2011**, *99*, 052107.
- [24] E. Guilmeau, A. Maignan, C. Wan, K. Koumoto, *Phys. Chem. Chem. Phys.* **2015**, *17*, 24541.
- [25] E. Guilmeau, T. Barbier, A. Maignan, D. Chateigner, *Appl. Phys. Lett.* **2017**, *111*, 133903.
- [26] J. Li, Q. Tan, J.-F. Li, *J. Alloys Compd.* **2013**, *551*, 143.
- [27] C. Bourgès, P. Lemoine, O. I. Lebedev, R. Daou, V. Hardy, B. Malaman, E. Guilmeau, *Acta Mater.* **2015**, *97*, 180.
- [28] K. Hashikuni, K. Suekuni, K. Watanabe, Y. Bouyrie, M. Ohta, M. Ohtaki, T. Takabatake, *J. Solid State Chem.* **2018**, *259*, 5.
- [29] C. Bourgès, V. Pavan Kumar, H. Nagai, Y. Miyazaki, B. Raveau, E. Guilmeau, *J. Alloys Compd.* **2019**, *781*, 1169.
- [30] T. Barbier, D. Berthebaud, R. Frésard, O. I. Lebedev, E. Guilmeau, V. Eyert, A. Maignan, *Inorg. Chem. Front.* **2017**, *4*, 424.
- [31] E. Rathore, R. Juneja, S. P. Culver, N. Minafra, A. K. Singh, W. G. Zeier, K. Biswas, *Chem. Mater.* **2019**, *31*, 2106.
- [32] G. Tan, S. Hao, J. Zhao, C. Wolverton, M. G. Kanatzidis, *J. Am. Chem. Soc.* **2017**, *139*,

6467.

- [33] E. J. Skoug, D. T. Morelli, *Phys. Rev. Lett.* **2011**, *107*, 235901.
- [34] A. Sugaki, H. Shima, A. Kitakaze, *Technol. Report, Yamaguchi Univ. Yamaguchi, Japan* **1972**, *I*, 76.
- [35] Z.-Z. Luo, C.-S. Lin, W.-D. Cheng, W.-L. Zhang, Y.-B. Li, Y. Yang, H. Zhang, Z.-Z. He, *Cryst. Growth Des.* **2013**, *13*, 4118.
- [36] B. Schmitt, C. Brönnimann, E. F. Eikenberry, F. Gozzo, C. Hörmann, R. Horisberger, B. Patterson, *Nucl. Instruments Methods Phys. Res. A* **2003**, *501*, 267.
- [37] E. Suard, A. Hewat, *Neutron News* **2001**, *12*, 30.
- [38] G. Caglioti, A. Paoletti, F. P. Ricci, *Nucl. Instruments* **1958**, *3*, 223.
- [39] J. Rodríguez-Carvajal, *Phys. B* **1993**, *192*, 55.
- [40] T. Roisnel, J. Rodríguez-Carvajal, *Mater. Sci. Forum* **2001**, *378-381*, 118.
- [41] P. Thompson, D. E. Cox, J. B. Hastings, *J. Appl. Crystallogr.* **1987**, *20*, 79.
- [42] E. Alleno, D. Bérardan, C. Byl, C. Candolfi, R. Daou, R. Decourt, E. Guilmeau, S. Hébert, J. Hejtmanek, B. Lenoir, P. Masschelein, V. Ohorodnichuk, M. Pollet, S. Populoh, D. Ravot, O. Rouleau, M. Soulier, *Rev. Sci. Instrum.* **2015**, *86*, 011301.
- [43] G. Kresse, J. Furthmüller, *Comput. Mater. Sci.* **1996**, *6*, 15.
- [44] G. Kresse, J. Furthmüller, *Phys. Rev. B* **1996**, *54*, 11169.
- [45] J. P. Perdew, K. Burke, M. Ernzerhof, *Phys. Rev. Lett.* **1996**, *77*, 3865.
- [46] S. L. Dudarev, G. A. Botton, S. Y. Savrasov, C. J. Humphreys, A. P. Sutton, *Phys. Rev. B* **1998**, *57*, 1505.
- [47] H. J. Monkhorst, J. D. Pack, *Phys. Rev. B* **1976**, *13*, 5188.
- [48] R. Dronskowski, P. E. Bloechl, *J. Phys. Chem.* **1993**, *97*, 8617.
- [49] V. L. Deringer, A. L. Tchougréeff, R. Dronskowski, *J. Phys. Chem. A* **2011**, *115*, 5461.
- [50] S. Maintz, V. L. Deringer, A. L. Tchougréeff, R. Dronskowski, *J. Comput. Chem.* **2013**,

- 34, 2557.
- [51] S. Maintz, V. L. Deringer, A. L. Tchougréeff, R. Dronskowski, *J. Comput. Chem.* **2016**, *37*, 1030.
- [52] S. J. Clark, M. D. Segall, C. J. Pickard, P. J. Hasnip, M. I. J. Probert, K. Refson, M. C. Payne, *Z. Krist.* **2005**, *220*, 567.
- [53] J. P. Perdew, A. Ruzsinszky, G. I. Csonka, O. A. Vydrov, G. E. Scuseria, L. A. Constantin, X. Zhou, K. Burke, *Phys. Rev. Lett.* **2008**, *100*, 136406.
- [54] E. Makovicky, W. G. Mumme, J. A. Watts, *Can. Mineral.* **1977**, *15*, 339.
- [55] E. Makovicky, W. H. Paar, H. Putz, G. Zagler, *Can. Mineral.* **2010**, *48*, 467.
- [56] V. Kupčik, *Handbook of Geochemistry, Vol. II/3*; Wedepohl, K. H., Ed.; Springer-Verlag Berlin Heidelberg, 1972.
- [57] S. Azam, S. A. Khan, S. Goumri-Said, M. B. Kanoun, *J. Electron. Mater.* **2017**, *46*, 23.
- [58] A. F. May, E. S. Toberer, A. Saramat, G. J. Snyder, *Phys. Rev. B* **2009**, *80*, 125205.
- [59] E. S. Toberer, A. Zevalkink, N. Crisosto, G. J. Snyder, *Adv. Funct. Mater.* **2010**, *20*, 4375.
- [60] B. Xu, T. Feng, M. T. Agne, Q. Tan, Z. Li, K. Imasato, L. Zhou, J.-H. Bahk, X. Ruan, G. J. Snyder, Y. Wu, *Angew. Chemie - Int. Ed.* **2018**, *57*, 2413.
- [61] L.-D. Zhao, V. P. Dravid, M. G. Kanatzidis, *Energy Environ. Sci.* **2014**, *7*, 251.
- [62] G. Tan, L.-D. Zhao, M. G. Kanatzidis, *Chem. Rev.* **2016**, *116*, 12123.
- [63] H.-S. Kim, Z. M. Gibbs, Y. Tang, H. Wang, G. J. Snyder, *APL Mater.* **2015**, *3*, 041506.
- [64] D. T. Morelli, V. Jovovic, J. P. Heremans, *Phys. Rev. Lett.* **2008**, *101*, 035901.
- [65] J. K. Lee, M.-W. Oh, B. Ryu, J. E. Lee, B.-S. Kim, B.-K. Min, S.-J. Joo, H.-W. Lee, S.-D. Park, *Sci. Rep.* **2017**, *7*, 4496.
- [66] K. Kurosaki, A. Kosuga, H. Muta, M. Uno, S. Yamanaka, *Appl. Phys. Lett.* **2005**, *87*, 061919.

- [67] J. Li, J. Sui, C. Barreateau, D. Berardan, N. Dragoe, W. Cai, Y. Pei, L.-D. Zhao, *J. Alloys Compd.* **2013**, *551*, 649.
- [68] S. K. Saha, G. Dutta, *Phys. Rev. B* **2016**, *94*, 125209.
- [69] L. Pan, Q. Xia, S. Ye, N. Ding, Z. Liu, *Trans. Nonferrous Met. Soc. China* **2012**, *22*, 1197.
- [70] L.-D. Zhao, J. He, D. Berardan, Y. Lin, J.-F. Li, C.-W. Nan, N. Dragoe, *Energy Environ. Sci.* **2014**, *7*, 2900.
- [71] Y. Pei, C. Chang, Z. Wang, M. Yin, M. Wu, G. Tan, H. Wu, Y. Chen, L. Zheng, S. Gong, T. Zhu, X. Zhao, L. Huang, J. He, M. G. Kanatzidis, L.-D. Zhao, *J. Am. Chem. Soc.* **2016**, *138*, 16364.
- [72] T. Zhou, B. Lenoir, M. Colin, A. Dauscher, R. Al Rahal Al Orabi, P. Gougeon, M. Potel, E. Guilmeau, *Appl. Phys. Lett.* **2016**, *98*, 162106.
- [73] X. Liu, D. Wang, H. Wu, J. Wang, Y. Zhang, G. Wang, S. J. Pennycook, L.-D. Zhao, *Adv. Funct. Mater.* **2019**, *29*, 1806558.
- [74] X. Gao, M. Zhou, Y. Cheng, G. Ji, *Philos. Mag.* **2016**, *96*, 208.
- [75] J.-B. Labégorre, R. Al Rahal Al Orabi, A. Virfeu, J. Gamon, P. Barboux, L. Pautrot-d'Alençon, T. Le Mercier, D. Berthebaud, A. Maignan, E. Guilmeau, *Chem. Mater.* **2018**, *30*, 1085.
- [76] R. Al Rahal Al Orabi, P. Gougeon, P. Gall, B. Fontaine, R. Gautier, M. Colin, C. Candolfi, A. Dauscher, J. Hejtmanek, B. Malaman, B. Lenoir, *Inorg. Chem.* **2014**, *53*, 11699.
- [77] J. Y. Cho, X. Shi, J. Yang, *Phys. Rev. B* **2011**, *84*, 085207.
- [78] M. D. Nielsen, V. Ozolins, J. P. Heremans, *Energy Environ. Sci.* **2013**, *6*, 570.
- [79] W. Lai, Y. Wang, D. T. Morelli, X. Lu, *Adv. Funct. Mater.* **2015**, *25*, 3648.
- [80] W. G. Zeier, A. Zevalkink, Z. M. Gibbs, G. Hautier, M. G. Kanatzidis, G. J. Snyder, Thinking Like a Chemist: Intuition in Thermoelectric Materials. *Angew. Chemie - Int. Ed.* **2016**, *55*, 6826–6841.

- [81] P. Debye, *Ann. Phys.* **1912**, 344, 789.
- [82] G. A. Slack, *J. Phys. and Chem. Solids* **1973**, 34, 321.
- [83] H. Lin, G. Tan, J.-N. Shen, S. Hao, L.-M. Wu, N. Calta, C. Malliakas, S. Wang, C. Uher, C. Wolverton, M. G. Kanatzidis, *Angew. Chemie - Int. Ed.* **2016**, 55, 11431.
- [84] P. Vaqueiro, R. Al Rahal Al Orabi, S. D. N. Luu, G. Guélou, A. V Powell, R. I. Smith, J.-P. Song, D. Wee, M. Fornari, *Phys. Chem. Chem. Phys.* **2015**, 17, 31735.
- [85] M. Christensen, A. B. Abrahamsen, N. B. Christensen, F. Juranyi, N. H. Andersen, K. Lefmann, J. Andreasson, C. R. H. Bahl, B. B. Iversen, *Nat. Mater.* **2008**, 7, 811.
- [86] D. Volja, B. Kozinsky, A. Li, D. Wee, N. Marzari, M. Fornari, *Phys. Rev. B - Condens. Matter Mater. Phys.* **2012**, 85, 245211.
- [87] D. Wee, B. Kozinsky, M. Fornari, *J. Phys. Soc. Japan* **2013**, 82, 014602.
- [88] R. Al Rahal Al Orabi, E. Orisakwe, D. Wee, B. Fontaine, R. Gautier, J.-F. Halet, M. Fornari, *J. Mater. Chem. A* **2015**, 3, 9945.
- [89] D. G. Cahill, S. K. Watson, R. O. Pohl, *Phys. Rev. B* **1992**, 46, 6131.
- [90] R. Al Rahal Al Orabi, J. Hwang, C.-C. Lin, R. Gautier, B. Fontaine, W. Kim, J.-S. Rhyee, D. Wee, M. Fornari, *Chem. Mater.* **2017**, 29, 612.
- [91] R. Al Rahal Al Orabi, N. A. Mecholsky, J. Hwang, W. Kim, J. Rhyee, D. Wee, M. Fornari, *Chem. Mater.* **2016**, 28, 376.
- [92] H. Wang, J. Hwang, M. L. Snedaker, I. Kim, C. Kang, J. Kim, G. D. Stucky, J. Bowers, W. Kim, *Chem. Mater.* **2015**, 27, 944.
- [93] H. Wang, J.-H. Bahk, C. Kang, J. Hwang, K. Kim, A. Shakouri, W. Kim, *J. Mater. Chem. A* **2013**, 1, 11269.
- [94] K. Biswas, J. He, I. D. Blum, C.-I. Wu, T. P. Hogan, D. N. Seidman, V. P. Dravid, M. G. Kanatzidis, *Nature* **2012**, 489, 414.

Table of Content

Jean-Baptiste Labégorre, Agathe Virfeu, Abdelhamid Bourhim, H elo ise Willeman, Tristan Barbier, Florian Appert, Jean Juraszek, Bernard Malaman, Arthur Huguenot, R egis Gautier, Vivian Nassif, Pierric Lemoine, Carmelo Prestipino, Erik Elkaim, Lauriane Pautrot-d'Alen on, Thierry Le Mercier, Antoine Maignan, Rabih Al Rahal Al Orabi, Emmanuel Guilmeau

A new cost-efficient *n*-type layered thermoelectric material with ultralow thermal conductivity. Correlation between structure, transport properties, electronic band structure and phonon calculations.

